NANO LETTERS

Letter

pubs.acs.org/NanoLett

Fully Crystalline Faceted Fe–Au Core–Shell Nanoparticles

C. Langlois,[†,∥] P. Benzo,[†] R. Arenal,[‡,§] M. Benoit,[†] J. Nicolai,[†] N. Combe,[†] A. Ponchet,[†] and M. J. Casanove*[,†]

[†]CEMES, CNRS UPR 8011 and Université de Toulouse, 29 rue Jeanne Marvig, F-31055 Toulouse, France
[‡]L.M.A., Instituto de Nanociencia de Aragon, Universidad de Zaragoza, C/Mariano Esquillor s/n, 50018 Zaragoza, Spain
[§]Fundacion ARAID, 50018 Zaragoza, Spain

S *Supporting Information*

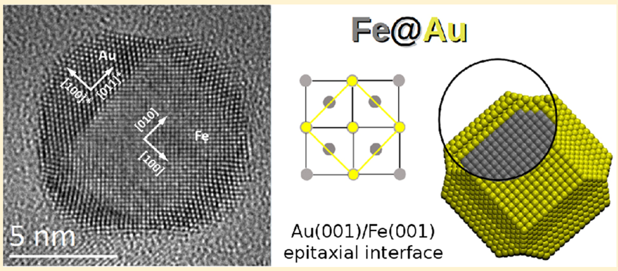

ABSTRACT: Fe–Au core–shell nanoparticles displaying an original polyhedral morphology have been successfully synthesized through a physical route. Analyses using transmission electron microscopy show that the Au shell forms truncated pyramids epitaxially grown on the (100) facets of the iron cubic core. The evolution of the elastic energy and strain field in the nanoparticles as a function of their geometry and composition is calculated using the finite-element method. The stability of the remarkable centered core–shell morphology experimentally observed is attributed to the weak elastic energy resulting from the low misfit at the Fe/Au (100) interface compared to the surface energy contribution.

KEYWORDS: *core–shell nanocrystals, equilibrium structure, iron–gold epitaxy, PVD growth, transmission electron microscopy*

Among the different possible distributions of two metals in a nanoparticle (NP), the core–shell chemical order is particularly valuable as it takes advantage of the properties of the two different metals, whereas its particular morphology helps to prevent the core metal from oxidation. Such heterostructures display unique electronic properties, enhanced reactivity, and easier functionalization.[1–5] Different properties, such as catalytic reactivity—including photocatalysis[6]—or electrical conductivity,[7] for instance, are also known to be dependent on the NP morphology and especially on the presence of crystalline facets. Faceted core–shell NPs are thus highly desirable.

The stability and consequently the equilibrium shape of core–shell nanocrystals are still largely unknown. In monometallic nanocrystals, the equilibrium shape, described by the well-known Wulff construction,[8] results from the minimization of the orientation-dependent surface free energy. Similar construction was proposed for metallic alloy nanocrystals and gave evidence of a size dependency of the equilibrium shape.[9] The case of bimetallic NPs with separated domains, as core–shell nanocrystals, is even more complex. In addition to the mentioned size effect, which presumably still operates, the strong interaction between the two metallic domains prevents a straightforward determination of their equilibrium shape. The complex interplay between structure, geometry, and chemical ordering in core–shell or Janus-like NPs was thus recently pointed out.[10,11]

In this paper, we focus on the synthesis and the stability of faceted Fe–Au core–shell nanocrystals. The Fe–Au system indeed presents suitable properties for synthesizing core–shell nanocrystals. The large difference in surface energies, 1.500 J·m^{-2} for (111) Au compared to 2.417 J·m^{-2} for (100) Fe (experimental values)[12] should promote Au free surface segregation. Besides, despite the structural dissimilarity of body-centered cubic (bcc) iron and face-centered cubic (fcc) gold, and a large difference in lattice parameters (a_{Fe} = 0.28665 nm for Fe and a_{Au} = 0.40784 nm for Au, values taken from Okamoto et al.[13]), Au can grow epitaxially on a (100) iron plane with the following orientation relationship Au (100) [011]//Fe(100)[010]. In a previous paper,[14] we investigated the structural and electronic properties of this particular interface through density functional theory (DFT) calculations. The value of the Au (100)/Fe(100) interface energy was found as low as 356 mJ·m^{-2}, favoring the coverage of (100) iron facets by gold.

Combining a magnetic core with a biocompatible, chemically inert, and easily functionalized shell, Fe@Au core–shell NPs are promising candidates for biomedical applications, as far as the Au shell provides an efficient coverage of the toxic Fe core.[15] Such NPs benefit from the superior properties of Fe compared to its oxides to be manipulated (for drug delivery) or heated (for destroying tumors through hyperthermia) as well as to provide enhanced contrast in magnetic resonance imaging (MRI).[16] Thus, in recent years, much attention has been paid to the synthesis and properties of Fe–Au core–shell NPs both theoretically[4] and experimentally.[17–21] Most of these studies report chemically synthesized Fe–Au NPs, formed by an assembly of nanograins and displaying a rounded shape. Using

Received: March 26, 2015
Revised: June 30, 2015

DOI: 10.1021/acs.nanolett.5b02273

solid-state dewetting of thin Fe/Au films at high temperature, Amram et al. recently succeeded in growing large [110]-oriented monocrystalline Fe islands encapsulated in a thin Au film.[22]

Controlling the structure and geometry of Fe−Au core−shell nanocrystals however remains a major issue to take full advantage of the properties of each metal in its crystalline state and to protect both Fe from oxidation and cells from Fe toxicity. Besides, due to facet-specific binding of organic molecules,[23] shaping of the gold shell is essential to control the interaction between the NP and its organic environment.

Here, we report the successful synthesis of Fe−Au bimetallic crystalline NPs adopting an original polyhedral core−shell morphology in which a Fe nanocube core acts as a nanosubstrate for the epitaxial growth of gold islands with a truncated pyramid shape. First, we detail the synthesis of these Fe−Au NPs, about 13 nm large, through a physical route and their structural, geometrical, and chemical characterization by transmission electron microscopy (TEM) and related techniques at the atomic level. The origin of their highly symmetrical morphology is then investigated with special focus on the respective part played by elastic and surface energies (see Supporting Information for more details on synthesis, characterization, and finite-element analysis).

Fe−Au NPs were grown by sequential deposition from two elemental targets in an ultrahigh vacuum sputtering device. A NaCl (100) crystal was used as a substrate and covered by a 5 nm thick amorphous alumina layer. The metallic layers, with nominal thicknesses of 2 nm for iron and 1 nm for Au, were then deposited at 800 °C (substrate temperature measured in our setup) in order to ensure the formation of Fe NPs and to favor the diffusion of gold atoms or small clusters toward the Fe NPs. After metal deposition, the temperature was slowly decreased to room temperature and maintained at this temperature to deposit a 5 nm thick alumina cover layer in order to prevent oxidation and NPs coalescence. After dissolution of the NaCl substrate, the Fe−Au NPs embedded in the alumina matrix were deposited on copper grids for TEM investigations. Figure 1 displays a general view of the grown NPs recorded in a high-angle annular dark-field scanning transmission electron microscopy (HAADF-STEM) mode. The corresponding size distribution histogram, displayed in Figure 1, was fitted with a log-normal function with a mean value of 12.8 nm and a standard deviation of 2.8 nm. The histogram thus reveals a narrow size dispersity, despite the unavoidable coalescence of some NPs leading to the larger NPs sizes reported in the histogram. Thanks to the Z-contrast, available in HAADF-STEM mode, the dark-core/bright-shell distribution observed in most of the NPs can be undoubtedly attributed to an Fe-rich core and a Au-rich shell, respectively. Moreover, these NPs display a well-defined morphology with a cubic Fe core and a shell formed of Au pyramidal islands when they are suitably oriented, that is, when they are observed along one of the Fe cube facets (note that the NPs are randomly oriented in the alumina matrix). One of these NPs is displayed in the inset of Figure 1. Interestingly, pure Fe NPs grown in the same conditions mostly exhibit a rounded shape, and the cubic morphology only appears after Au coverage (see S1 in Supporting Information).

The chemical composition of the core and pyramid regions of several NPs was analyzed by energy dispersive X-ray spectrometry (EDS). Figure 2 presents the EDS spectra recorded in two different regions of a small nanoparticle. Due to the presence of top and bottom Au pyramids, the spectrum recorded in the core region displays both Fe and Au peaks. On the contrary, only the Au peaks are clearly observed in the pyramid region. Of course, Fe traces in Au (or Au traces in Fe) can remain undetected because of a very low signal-to-noise ratio. However, interdiffusion of the two species is only expected at high temperature or in size-constrained systems[24,25] and the slow decrease of the temperature during the synthesis process (prior to the deposition of the cover layer) will promote phase separation (fcc Au and bcc Fe). Indeed, the miscibility of Au in bcc Fe is already as low as 0.1 at. % at 500 °C (ref 26 and included references). The HAADF-STEM image displayed in Figure 2 clearly reveals the existence of two different crystal lattices (one in the core region and one in the surrounding pyramids). In order to go further in the structural analysis, and in particular to clearly identify the two different

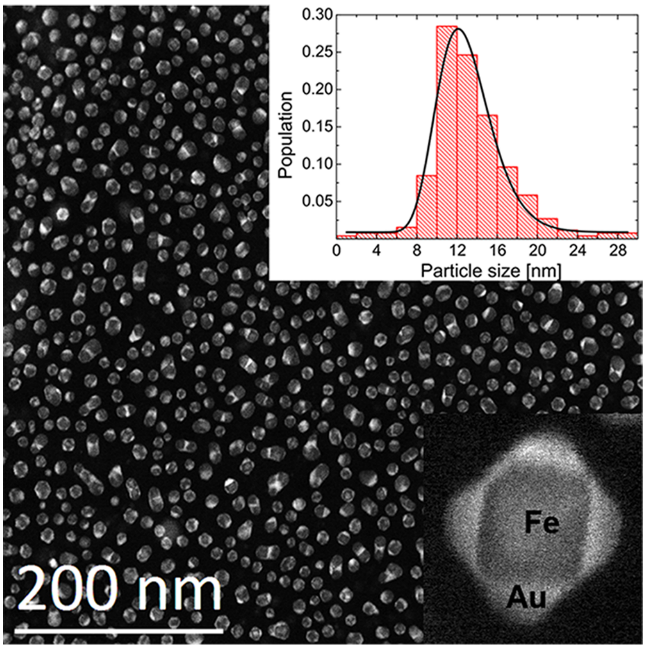

Figure 1. As-grown Fe−Au NPs observed in HAADF-STEM mode. The corresponding size distribution of the NPs is displayed in inset together with an enlarged view of one of the numerous NPs presenting a very regular core−shell morphology with an easily recognizable square-shaped core.

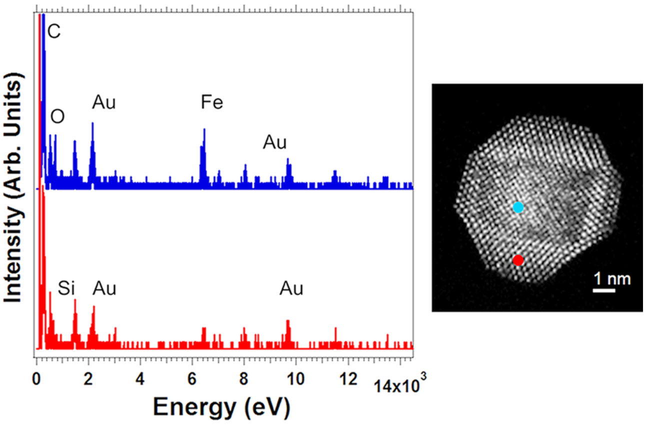

Figure 2. Left: EDS spectra recorded respectively in the core (top) and shell (bottom) regions of the NP displayed on the right. Right: HAADF-STEM image of the corresponding Fe−Au NP.

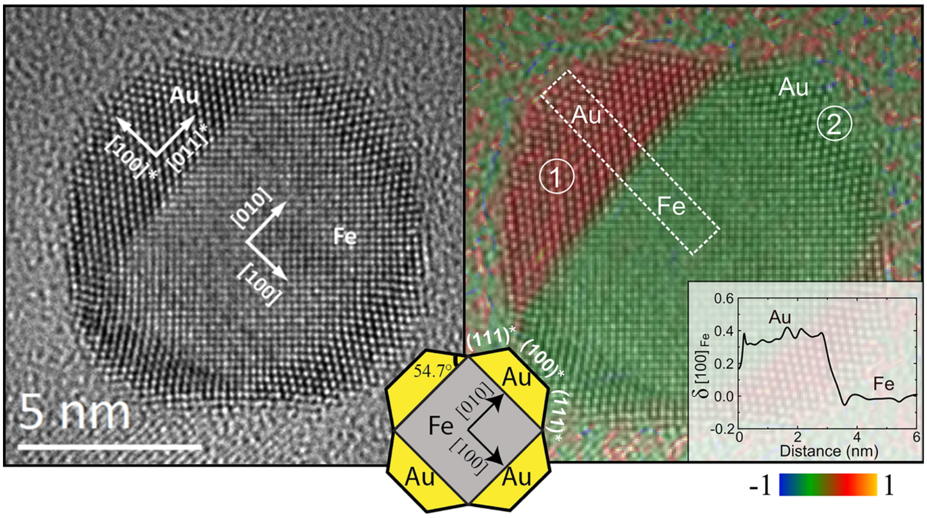

Figure 3. Left: HREM micrograph of a core−shell NP and corresponding scheme. The directions and planes labeled with a star (*) correspond to the Au structure. Right: same micrograph superimposed to the map of $\delta_{[100]}$ measured by geometrical phase analysis (color online). The line profile along the [100] Fe axis, taken from the rectangular region, is plotted in the inset.

lattices, the NPs were also studied in Cs-corrected high-resolution TEM (HREM). Note that in this mode, the contrast of the atomic columns in the iron core can be optimized by changing the focus conditions, thus imaging the central region of the NP, despite the presence of gold pyramids on the upper and lower faces of the Fe core. Low Si contribution should be due to some contamination. A typical HREM image of a suitably oriented NP is displayed in Figure 3. The analysis of the diffractograms (Fourier transforms) corresponding to the core and the pyramids confirms that both regions are formed by nanocrystals (not shown). The Fe nanocrystal, in its bcc phase, is observed along a [001] axis and displays a nanocube shape exposing {100} facets. The fcc Au nanocrystals, observed along their $[01\bar{1}]$ axis, present a truncated pyramid morphology with top and bottom bases parallel to (100) planes and lateral facets parallel to (111) planes. The scheme in Figure 3 sums up this structural and morphological analysis. It is worth noticing that the concavity of the Au surface is directly related to the presence of the Fe cube corners and more precisely to the angle of 160.6° between (111) Au facets of two adjacent truncated pyramids.

The lattice parameter in the Au pyramids was better determined using the geometrical phase analysis method (GPA).[27] In this method, the analyzed region, here the Au pyramid, is considered as a strained version of the reference region, chosen in the Fe region in our case. The colored map superimposed to the HREM image in Figure 3 (color online) displays the variation ($\delta_{[100]}$) of the lattice plane spacing in a given region compared to the (100) lattice plane spacing in the center of the iron core. The line profile along the [100] Fe axis, displayed in inset, shows an abrupt increase of $\delta_{[100]}$, around 40%, when crossing the interface from the Fe core to pyramid 1. This measured variation well agrees with the important relative change in lattice parameters $(a_{\mathrm{Au}} - a_{\mathrm{Fe}})/a_{\mathrm{Fe}}$. In pyramid 2, which is differently oriented relatively to the Fe lattice, the measured lattice spacing corresponds to the spacing of a {110}* Au plane family (the * referring to the Au lattice). The absence of contrast at this interface clearly reveals the coherent epitaxial growth of the Au pyramids over the Fe cube facets.

In summary, the Au shell has epitaxially grown on the Fe {100} cube facets following the previously mentionned orientation relationship. The misfit parameter at the interface plane defined as $f = (a_{\mathrm{Au}} - a_{\mathrm{Fe}}\sqrt{2})/a_{\mathrm{Au}} = 0.6\%$ is weak, favoring the easy growth of gold under a slight in-plane compressive strain.

In order to understand the stability of this highly symmetrical morphology, especially compared to an asymmetric Janus-like morphology, the shape-dependency of the NP energy is evaluated in the following through the computation of the elastic and surface energies. Though, in principle, the substrate influences the observed NP morphology,[28,29] the use of an amorphous alumina substrate prevents any significant elastic transfer from the substrate to the NP. Besides, interface energies promote a gold/alumina interface[30] and gold weakly wets alumina. The effect of the substrate on the equilibrium NP shape, thus, is expected to be at most a slight truncation of the gold shell.[31] Hence, in the following, calculations are performed on unsupported NPs.

The normalized NP elastic energy $\tilde{E}_{\mathrm{el}} = E_{\mathrm{el}}/E_{\mathrm{2D}}$ was calculated by the finite-element method (FEM) in the frame of anisotropic elasticity. E_{el} is the elastic energy in the NP and E_{2D} is the elastic energy stored in a Au 2D layer (with same Au volume as in the NP) homogeneously strained with an in-plane biaxial strain $\epsilon_{\parallel} = -f$ and free of out-of-plane stress (See Supporting Information for more details on the finite-element analysis). The values of Fe and Au elastic constants used in the calculation are the experimental ones measured at 300 K.[32,33]

The observed core−shell symmetrical morphology is modeled by an iron cube with edge b of 8 nm (consistent with the NP displayed in Figure 3), surrounded by six identical Au truncated pyramids with height h (with h varying from 0.8 to 2.4 nm, i.e., for $h/b = 0.1$, 0.2, and 0.3). Note that the quantity h/b is also reminiscent of the relative gold volume compared to the Fe one. The crystallographic orientations of the truncated pyramids correspond to the ones experimentally observed and, in agreement with the results of the GPA analysis, the pyramids are coherently strained on the Fe core. The stability of the core−shell morphology is investigated by computing the evolution of the normalized elastic energy $\tilde{E}_{\mathrm{el}}$ along a shape transition to a Janus-like morphology: the height of five out of six pyramids is progressively decreased while the height of the sixth pyramid h_{h} increases, for a given Au volume (the Fe volume remaining constant). The ratio h_h/b ranging from h/b to 0.7 (i.e., the value corresponding to the untruncated pyramid, given the pyramid angle of 54.7°) plays the role of an order parameter to describe the shape transition.

From FEM, we found that $\tilde{E}_{el}$ is less than 1 in all investigated morphologies. This demonstrates that the elastic energy E_{el} in the NP is relaxed compared to the energy of the 2D layer, E_{2D}. Moreover, the calculations showed that about 10% of E_{el} is supported by the iron deformation. Thus, the relaxation of the elastic energy is due, not only to the free surfaces of the truncated pyramids, but also to the transfer of a part of the elastic strain from the Au shell to the Fe core. The situation is very close to the mechanism involved in the island growth mode usually observed in mismatched heterostructures.[34]

Figure 4 reports the normalized elastic energy $\tilde{E}_{el}$ as a function of h_h/b, for three different relative Au volumes. For the smallest relative Au volume considered here, $h/b = 0.1$, the six truncated pyramids are four Au monolayers (ML) high in the fully symmetrical core−shell chemical distribution $h_h/b = h/b$. In this situation, about 20% of the elastic energy is released compared to an unrelaxed 2D Au layer. The normalized elastic energy $\tilde{E}_{el}$ decreases as the NP adopts an asymmetrical configuration. In the extreme configuration ($h_h/b = 0.7$), about 30% of the elastic energy is released. For the largest Au volume, $h/b = 0.3$, which is close to the experimentally observed NPs, 40% of the elastic energy is released and $\tilde{E}_{el}$ remains almost independent of h_h/b. Thus, the elastic energy tends to favor asymmetrical Janus-like chemical configurations, especially for small Au volumes. Clearly, these effects originate from the strain distribution inside the pyramids.

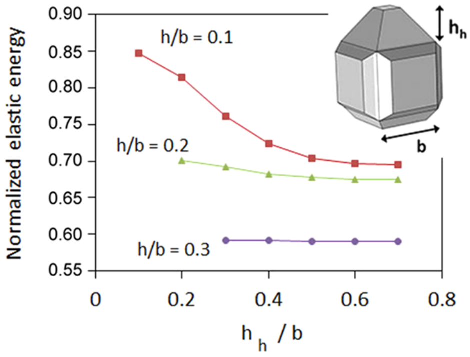

Figure 4. Evolution of the normalized elastic energy $\tilde{E}_{el}$ in Fe−Au NPs with a cubic iron core (edge b) and a gold shell formed by six truncated pyramids when one of the pyramid (height h_h) grows at the expense of the five others (as represented in the inset). Calculations were done for: $b = 8$ nm, $f = 0.6\%$, and $h/b = 0.1$, 0.2, and 0.3.

Figure 5 displays a map of the ϵ_{zz} strain component (i.e., along the vertical axis of the figure) inside NPs containing the smallest and largest relative gold volume for both the symmetrical and asymmetrical configurations. Inside the truncated or untruncated pyramids, ϵ_{zz} corresponds either to the out-of-plane strain $\epsilon_\perp$ or to the in-plane strain $\epsilon_\parallel$ component, depending on the pyramid position (top/bottom or side).

For the smallest relative gold volume in the symmetrical configuration ($h_h/b = h/b = 0.1$, Figure 5a), the strain field in gold truncated pyramids remains nearly homogeneous and close to the theoretical values for the 2D layer given by $\epsilon_\parallel = -f = -0.006$ and $\epsilon_\perp = (2C_{12}/C_{11}) \cdot f = 0.0102$. On the contrary, in the asymmetrical configuration ($h/b = 0.1$ and $h_h/b = 0.7$, Figure 5b), the Au volume transferred from the lower truncated pyramids to the untruncated one benefits from a much larger elastic relaxation. Especially, in the untruncated pyramid, $\epsilon_\perp$ is close to zero beyond a distance of about 0.3 b from the interface. The same occurs for $\epsilon_\parallel$ (not shown). For the largest relative gold volume $h/b = 0.3$, the top of the truncated pyramids is already relaxed (Figure 5c) in the symmetrical configuration $h_h/b = h/b = 0.3$, explaining (i) the smaller normalized elastic energy $\tilde{E}_{el}$ than with $h_h/b = h/b = 0.1$, as displayed in Figure 4 and (ii) the fact that removing a small amount of Au from five truncated pyramids to complement the sixth one (Figure 5d) does not significantly change the elastic energy. This also shows that the most external atomic layers of the experimental NPs (closed from the configuration $h/b = h_h/b = 0.3$) are practically free of stress.

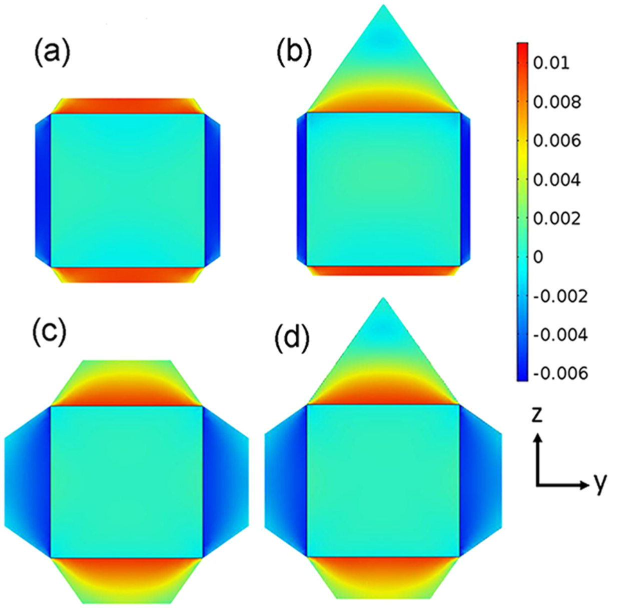

Figure 5. (color online) Mapping of the ϵ_{zz} strain component displayed along the central cross section of a NP (at $x = b/2$) in NPs with two different Au volumes corresponding to top, $h/b = 0.1$ (a and b); bottom $h/b = 0.3$ (c and d). For each Au volume, we compare fully symmetrical $h_h/b = h/b$ (a) and (c) and asymmetrical $h_h/b = 0.7$ (b) and (d) nanoparticles. Note that the ϵ_{zz} component corresponds to the out-of plane strain for the top and bottom Au pyramids, and to the in-plane strain component for the other pyramids.

Given the high surface/volume ratio in NPs, the volume elastic energy must be compared to the surface and interface energies. The surface energy E_s is calculated considering the surface energy 1.500 J·m^{-2} for (111)Au (experimental value from ref 12) and 1.800 J·m^{-2} for (100)Au. With the lack of experimental data, this last value is deduced from the ratio of (111) and (100) surface energy calculated by DFT.[14] As the Au/Fe interface energy remains unchanged when changing the shape from the symmetrical to the Janus-like configuration considered here, the NP total energy E is defined as the sum of the elastic and surface energies. Surface and interface stresses, not considered in this approximation, will be discussed below. Figure 6 reports the evolution of the NP total energy E as a function of the ratio h_h/b for the three relative gold volumes and for two different NP sizes $b = 8$ nm and $b = 800$ nm. For a NP size in the experimental range ($b = 8$ nm), the NP energy (Figure 6a) increases with h_h/b. Indeed, the surface energy

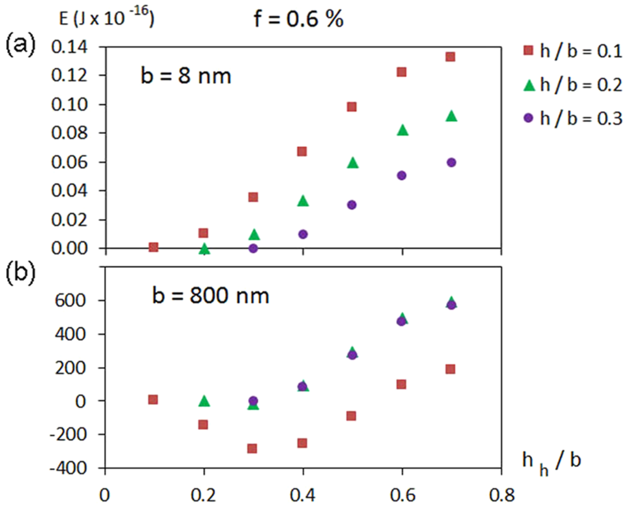

Figure 6. NP energy for a given Au volume referred as *h*/*b*, when the NP evolves from a fully symmetrical distribution of Au truncated pyramids to an asymmetrical distribution in which one of the pyramids grows at the expense of the five others: (a) for *b* = 8 nm; (b) for *b* = 800 nm.

monotonously increases from the symmetrical to the asymmetrical configuration and is about 2 orders of magnitude larger than the elastic energy. Nevertheless, as the surface and elastic energies scale, respectively, as b^2 and b^3, they are expected to compete for larger NP sizes. A NP size as big as b = 800 nm was necessary to find a minimum in the NP energy curve, as reported in Figure 6b for the smallest studied relative gold volume (h/b = 0.1).

These results demonstrate the enhanced stability of the Fe–Au core–shell with centered core in a wide range of NP size and for different shell thicknesses. The investigated Fe–Au NPs, thus, behave differently than already reported NPs formed in weakly miscible systems.[10,11] In the Ag–Cu system,[11] for instance, the stability of the core–shell geometry is strongly dependent on the shell thickness in NPs with size comparable to the Fe–Au NPs. Numerical calculations[10] performed on Au–Cu and related systems (Ag–Ni, Ag–Co, and Au–Co) showed that centered cores were unstable in crystalline core–shell NPs, whereas they were stable in icosaedral NPs. Two important characteristics of the core–shell NPs whose stability was investigated so far in the literature[35] are worth noticing: (i) the two metals crystallize in the same structure (typically fcc, including Co at small size) and (ii) there exists an important misfit between the two structures (as high as 11% in CuAg or even 14% in Au–Co for instance).

In the Fe–Au system, the low misfit at the (100) interface plays an important role in the morphology of the equilibrium configuration giving, over a wide range of NPs size, a prominent importance to surface energies. Indeed, imposing a large artificial misfit of 6% (not shown) in our FEM calculation, the total energy of a NP with b = 8 nm displays an energy minima favoring a slightly asymmetric morphology.

Our model includes a single type of Fe/Au interface. However, small (110) facets were sometimes observed at the cube edges of the Fe core. These facets, which dominate in the Wulff polyhedron for bcc crystals, will favor the formation of a Fe(110)/Au(111) interface with anisotropic lattice misfit.[36] The role of the gold shell on the morphology of the cubic iron core, and in particular on the development of the large (100) facets with low misfit experimentally observed at the expense of (110) facets with anisotropic misfit, has not yet been explored but will be considered in further studies.

Surface and interface stresses were not taken into account in the present study. Using DFT calculations, surface and interface stresses have been recently shown to be non negligible to predict the elastic state of Fe–Au NPs with sizes up to 20 nm.[37] However, the contribution of surface and interface stresses remains at most comparable to the one of the elastic energy for a 10 nm NP: its influence on the NP morphology (symmetric or Janus like) is thus expected to be very weak.

In summary, we achieved the synthesis of a new kind of core–shell Fe–Au NPs by a physical vapor deposition method. The TEM analysis of these highly faceted NPs demonstrated the epitaxial growth of strained Au pyramids on {100} Fe nanocube facets, ensuring an efficient protection of the core. The NP energy was calculated from fully symmetrical core–shell to asymmetrical Janus-like configurations. We showed that the remarkable stability of the Fe–Au NPs with centered core, in a large size range, was largely attributable to the low misfit at the Fe/Au (100) interface compared to other low miscible systems. Besides, FEM calculations also demonstrated that the state of strain at the exposed surface facets of the Au shell varies from fully strained to fully relaxed states depending on the NP morphology. These different results are of great interest for applications of core–shell magnetic nanoparticles. First, demonstrating that a complete gold shell can be grown on an iron nanocrystal, thus preventing the core from oxidation and ensuring biocompatibility of the NPs, provides a new design strategy for the biomedical field. Then, this morphology was found fully stable in the size range targeted in these applications. The control of key parameters as the nature and the state of strain of the exposed facets, as provided by this study, will be decisive for mastering surface properties of core–shell NPs, which is essential for further functionalization.

■ ASSOCIATED CONTENT

Ⓢ Supporting Information

See Supporting Information for synthesis details, and finite-element calculation details. The Supporting Information is available free of charge on the ACS Publications website at DOI: 10.1021/acs.nanolett.5b02273.

■ AUTHOR INFORMATION

Corresponding Author

*E-mail: casanove@cemes.fr.

Present Address

‖MATEIS, INSA Lyon, 7, Avenue Jean Capelle, 69621 Villeurbanne Cedex, France.

Notes

The authors declare no competing financial interest.

■ ACKNOWLEDGMENTS

We gratefully acknowledge the CNRS for having funded a one-year secondment position at CEMES to one of us (C.L.) and the European Associated Laboratory (LEA)–TALEM2 for financial support. The HR-STEM studies were conducted at the Laboratorio de Microscopias Avanzadas (L.M.A.) at Instituto de Nanociencia de Aragon, Universidad de Zaragoza, Spain. Part of this work was supported by the French Research National Agency under project Naïade ANR-11-BS10-017 and by the European Union Seventh Framework Program under

Grant Agreement 312483-ESTEEM2 (Integrated Infrastructure Initiative—I3). R.A. acknowledges funding from the Spanish Ministerio de Economia y Competitividad (FIS2013-46159-C3-3-P).

REFERENCES

(1) Cao, Y.; Jin, R.; Mirkin, C. A. *J. Am. Chem. Soc.* **2001**, *123*, 7961−7962.

(2) Sao-Joao, S.; Giorgio, S.; Penisson, J. M.; Chapon, C.; Bourgeois, S.; Henry, C. *J. Phys. Chem. B* **2005**, *109*, 342−347.

(3) Cazayous, M.; Langlois, C.; Oikawa, T.; Ricolleau, C.; Sacuto, A. *Phys. Rev. B: Condens. Matter Mater. Phys.* **2006**, *73*, 113402.

(4) Sun, Q.; Kandalam, A. K.; Wang, Q.; Jena, P.; Kawazoe, Y.; Marquez, M. *Phys. Rev. B: Condens. Matter Mater. Phys.* **2006**, *73*, 134409.

(5) Bao, Y.; Calderon, H.; Krishnan, K. M. *J. Phys. Chem. C* **2007**, *111*, 1941−1944.

(6) Yang, C.-W.; Chanda, K.; Lin, P.-H.; Wang, Y.-N.; Liao, C.-W.; Huang, M. H. *J. Am. Chem. Soc.* **2011**, *133*, 19993−20000.

(7) Wang, W.-C.; Lyu, L.-M.; Huang, M. H. *Chem. Mater.* **2011**, *23*, 2677−2684.

(8) Wulff, G. *Z. Kristallogr. - Cryst. Mater.* **1901**, *34*, 449−530.

(9) Ringe, E.; Van Duyne, R. P.; Marks, L. D. *Nano Lett.* **2011**, *11*, 3399−3403.

(10) Bochicchio, D.; Ferrando, R. *Phys. Rev. B: Condens. Matter Mater. Phys.* **2013**, *87*, 165435.

(11) Langlois, C.; Li, Z. L.; Yuan, J.; Alloyeau, D.; Nelayah, J.; Bochicchio, D.; Ferrando, R.; Ricolleau, C. *Nanoscale* **2012**, *4*, 3381−3388.

(12) Tyson, W.; Miller, W. *Surf. Sci.* **1977**, *62*, 267−276.

(13) Okamoto, H.; Massalski, T.; Swartzendruber, L.; Beck, P. *Bull. Alloy Phase Diagrams* **1984**, *5*, 592−601.

(14) Benoit, M.; Langlois, C.; Combe, N.; Tang, H.; Casanove, M.-J. *Phys. Rev. B: Condens. Matter Mater. Phys.* **2012**, *86*, 075460.

(15) Kayal, S.; Vijayaraghavan Ramanujan, R. *J. Nanosci. Nanotechnol.* **2010**, *10*, 1.

(16) Huber, D. *Small* **2005**, *1*, 482−501.

(17) Ban, Z.; Barnakov, Y. A.; Li, F.; Golub, V. O.; O'Connor, C. J. *J. Mater. Chem.* **2005**, *15*, 4660−4662.

(18) Cho, S.-J.; Shahin, A. M.; Long, G. J.; Davies, J. E.; Liu, K.; Grandjean, F.; Kauzlarich, S. M. *Chem. Mater.* **2006**, *18*, 960−967.

(19) Zhang, J.; Post, M.; Veres, T.; Jakubek, Z. J.; Guan, J.; Wang, D.; Normandin, F.; Deslandes, Y.; Simard, B. *J. Phys. Chem. B* **2006**, *110*, 7122.

(20) Naitabdi, A.; Ono, L. K.; Behafarid, F.; Cuenya, B. R. *J. Phys. Chem. C* **2009**, *113*, 1433−1446.

(21) Guo, X.; Brault, P.; Zhi, G.; Caillard, A.; Jin, G.; Guo, X. *J. Phys. Chem. C* **2011**, *115*, 24164.

(22) Amram, D.; Rabkin, E. *ACS Nano* **2014**, *8*, 10687−10693.

(23) Dong, L.; Luo, Q.; Cheng, K.; Shi, H.; Wang, Q.; Weng, W.; Han, W.-Q. *Sci. Rep.* **2014**, *4*, -..

(24) Velasco, C.; Pohl, D.; Surrey, A.; Bonatto-Minella, A.; Hernando, A.; Crespo, P.; Rellinghaus, B. *Nanotechnology* **2014**, *25*, 215703.

(25) Mukherjee, P.; Manchanda, P.; Kumar, P.; Zhou, L.; Kramer, M. J.; Kashyap, A.; Skomski, R.; Sellmyer, D.; Shield, J. E. *ACS Nano* **2014**, *8*, 8113.

(26) Milenkovic, S.; Schneider, A.; Hassel, A. *Gold Bull.* **2006**, *39*, 185−191.

(27) Hÿtch, M. J.; Snoeck, E.; Kilaas, R. *Ultramicroscopy* **1998**, *74*, 131−146.

(28) Müller, P.; Kern, R. *J. Cryst. Growth* **1998**, *193*, 257−270.

(29) Amram, D.; Rabkin, E. *Acta Mater.* **2013**, *61*, 4113−4126.

(30) Nicholas, M. *J. Mater. Sci.* **1968**, *3*, 571.

(31) Kaischew, R. *Commun. Bulg. Acad. Sci.(phys)* **1950**, *1*, 100−133.

(32) Neighbours, J. R.; Alers, G. A. *Phys. Rev.* **1958**, *111*, 707−712.

(33) Adams, J. J.; Agosta, D. S.; Leisure, R.; Ledbetter, H. *J. Appl. Phys.* **2006**, *100*, 113530.

(34) Ponchet, A.; Lacombe, D.; Durand, L.; Alquier, D.; Cardonna, J.-M. *Appl. Phys. Lett.* **1998**, *72*, 2984−2986.

(35) Habas, S. E.; Lee, H.; Radmilovic, V.; Somorjai, G. A.; Peidong, Y. *Nat. Mater.* **2007**, *6*, 692.

(36) Elmers, H.; Gradmann, U. *Surf. Sci.* **1994**, *304*, 201−207.

(37) Benoit, M.; Combe, N.; Ponchet, A.; Morillo, J.; Casanove, M.-J. *Phys. Rev. B: Condens. Matter Mater. Phys.* **2014**, *90*, 165437.